Key Points:
- Dynamics of the Xinmo landslide are estimated by inverting the force-time function from long-period seismic signals
- Accelerating, decelerating, and depositing processes are revealed by dynamic parameters, friction coefficient, and seismic signal features
- Relations between rapid processes and multiple preconditions of the chain-style landslide process are discussed by comprehensive analysis

Correspondence to:
Y. Chen and F. Liu,
yunchen@mail.iggcas.ac.cn;
liufeng@geomech.ac.cn

Chain-Style Landslide Hazardous Process: Constraints From Seismic Signals Analysis of the 2017 Xinmo Landslide, SW China

Wei Li[1,2] (ID), **Yun Chen[1,2]** (ID), **Feng Liu[3]** (ID), **Hongfeng Yang[4]** (ID), **Jianli Liu[5]**, and **Bihong Fu[6]** (ID)

[1]State Key Laboratory of Lithospheric Evolution, Institute of Geology and Geophysics, Chinese Academy of Sciences, Beijing, China, [2]Institutions of Earth Science, Chinese Academy of Sciences, Beijing, China, [3]Institute of Geomechanics, Chinese Academy of Geological Sciences, Beijing, China, [4]Earth System Science Programme, Faculty of Science, The Chinese University of Hong Kong, Hong Kong, China, [5]Geophysical and Geochemical Exploration Team, Shaanxi Geology and Mining Group, Xi'an, China, [6]Institute of Remote Sensing and Digital Earth, Chinese Academy of Sciences, Beijing, China

Abstract Landslides generally involve rapid acceleration and deceleration of huge mass in just several minutes, and their unpredictability have made real-time detections of their rapid processes difficult. Seismic signals generated by landslides provide an excellent opportunity to obtain the time-dependent observations on landslide's processes. We invert the force-time function by fitting long-period seismic signals generated by Xinmo landslide on 23 June 2017, SW China, and determine three-stage dynamic processes within 104-s duration of this event. Constrained by the field observed runout distance, we deduce the landslide's mass of about 9×10^9 kg with corresponding maximum velocity and acceleration of 58.8 m/s and 4.38 m/s^2, respectively. Combining dynamic parameters, apparent friction coefficient, and seismic signal features, we depict a dynamic landslide process initiated by high-position rockslide, traveled by rapid long runout debris, and deposited over an old landslide's deposition fan. The rapid process of the landslide is affected by multiple preconditions such as the structure, topography, and meteorology of the site, which is characteristic of a typical chain-style landslide hazard and could be helpful to recognize potential slope instabilities.

Plain Language Summary Rapid long-runout and large-volume landslides are dangerous geological hazards that often cause heavy losses of human lives and properties, and have been found in high mountain areas around the world. Factors that govern landslide's movement and catastrophic hazards are less well understood, one of the reasons being a lack of an effective method to learn about landslides' spatiotemporal processes. Through analysis of seismic signals generated by the Xinmo landslide on 23 June 2017, SW China, we deduce key features including mass, dynamic parameters, and apparent friction coefficient of the landslide, and we determine a three-stage dynamic process within 104-s duration of the typical chain-style landslide hazard governed by structural, topographical, and meteorological factors of the site. These results would make it possible to elucidate the physical processes of large and fast landslides, and help to estimate speed and scale of potential landslides in hazard assessments.

1. Introduction

Landslides, one of the most dangerous geological hazards in mountainous regions, are often characterized by rapid velocity, long runout, and large volume of mass movement (Cruden & Varnes, 1996). While basic kinematic features of landslides can be inferred from field observations after sliding, recovering the spatiotemporal process that is usually completed in just a few minutes is difficult. Moreover, physical processes governing energy dissipation during landslides remain uncertain, preventing accurate estimation of a few crucial factors in hazard assessments of landslides such as runout distance, covered area, and transporting velocity (Iverson et al., 2000; Keefer & Larsen, 2007; Lucas et al., 2014). Comprehensive investigation of the dynamic process of landslides not only has implications for their dynamics but also is helpful for assessing and managing catastrophic disasters (Ekström & Stark, 2013; Petley, 2013). Seismic signals are generated by landslides, as the slide mass accelerates, moves along the ground, decelerates to rest (Chao et al., 2016; Ekström & Stark, 2013; Fukao, 1995; Kanamori & Given, 1982; Takei & Kumazawa, 1994), and thus provide a potential way to remedy deficiencies of conventional observations (e.g., Allstadt, 2013; Chao

et al., 2017; Deparis et al., 2008; Ekström & Stark, 2013; Gualtieri & Ekström, 2017, 2018; Hibert et al., 2014; Schneider et al., 2010; Suriñach et al., 2005; Yamada et al., 2013).

On 23 June 2017 at about 21:39 UTC (5:39 am local time on 24 June), a catastrophic landslide occurred in Xinmo Village, Diexi Town, Maoxian County, Sichuan Province, SW China (Figure 1a), which resulted in a heavy loss of human lives and properties (10 deaths, 73 missing, and 103 houses completely destroyed). As revealed by postslide evidences from field observations (e.g., Dong et al., 2018; Fan, Xu, et al., 2017; Intrieri et al., 2018; Xu et al., 2017; Yin et al., 2017), this landslide is a typical high-position landslide with a local relief of 1,000–1,200 m and a long runout distance of ~2.4 km, whose source area detached from the top ridge of the Fugui Mountain at the highest altitude of 3,450 m with an estimated volume of 4.5×10^6 m^3, and deposited in the Songpinggou River at altitudes of 2,260–2,400 m with a total volume of 12×10^6 m^3 (Figure 1b).

The Xinmo Village is located at the eastern margin of Tibetan Plateau, which is a tectonically active mountain belt and was uplifted in late Cenozoic due to the ongoing India-Eurasia continental collision (Clark et al., 2005; Molnar & Tapponnier, 1975). Several strong earthquakes continually ruptured this area over the last few decades (e.g., 16–23 August 1976 M_w 6.7, 6.3, 6.4 Songpan earthquakes; 12 May 2008 M_w 7.9 Wenchuan earthquake, and 08 August 2017 M_w 6.5 Jiuzhaigou earthquake). In particular, the 1933 Diexi earthquake (M_w 7.3) happened just several kilometers away from the Xinmo Village and resulted in thousands of deaths in the landslide damming disaster (Figure 1a; Ren et al., 2018). The Xinmo Village is built on the deposits of an old landslide induced by the Diexi earthquake (Figure 1b; Fan, Xu, et al., 2017; Xu et al., 2017; Yin et al., 2017). Intense seismic activities and steep topographic relief, which are formed by crustal shortening and overthrusting in this area (Fu et al., 2011; Liu et al., 2017; Zhang et al., 2009), have been inferred as main predisposing factors of frequent geological disasters. Therefore, investigating relationships between preconditions on geological and meteorological time scales (approximately million years versus several months) and dynamic processes of disasters could be helpful for recognizing potential instabilities and mitigating catastrophic disasters.

In this study, we perform seismic signal analysis to provide more constraints on dynamic process of the Xinmo landslide. We invert the force-time function of this landslide by fitting long-period signals, and then determine its mass and dynamic parameters. Finally, based on the temporal correlation between seismic signals and inversion results, and analyzing combined with field observations, we provide a qualitative interpretation of relationship between multiple long-term preconditions and the dynamic process of the Xinmo landslide.

2. Data and Methods

2.1. Broadband Seismic Data

The 2017 Xinmo landslide generated strong seismic signals that were recorded by several seismic stations of the China National Seismic Network operated by the China Earthquake Administration (Figure 1a). These seismic signals are characterized by emergent onsets, long durations, no distinct body waves, and dominant surface waves (Figure 2a), which are distinct from regular earthquakes (Chao et al., 2016; Dammeier et al., 2011; Deparis et al., 2008; Hibert et al., 2011; Suriñach et al., 2005). Spectra of these seismic signals show two distinct amplitude peaks in high- and low-frequency bands (Figures 2b–2d), corresponding to different processes in landslides: long-period signals are related to bulk momentum variations of the whole slide mass, and high-frequency signals reflect momentum exchanges on smaller scales (Ekström & Stark, 2013; Hibert et al., 2011, 2017; Fukao, 1995; Kanamori & Given, 1982; Schneider et al., 2010). The onsets of these seismic signals are dominated by an impulse lasting ~10 s and overtaken by chaotic high-frequency signals, which are observable for stations at distance greater than 250 km (Figure 2a). The first onset was recorded by the closest station (MXI) with a distance of 45.6 km at 21:39:05 UTC. As shown in the waveform recorded at the MXI station, high-frequency signals' amplitude increases to peak motion at 21:39:45–21:40:20, and gradually fades into the background noise after 21:40:45, having a duration of ~100 s (Figure 2a).

From the available seismic data, we select 22 channel signals with good data quality (signal-to-noise ratio above 5.0 with average of 11.6) from 11 stations (Figures 1a and 2a; with distance ranges of 45.6–252.7 km) equipped with three-component broadband seismometers (CMG-3ESP 60 s—50 Hz or
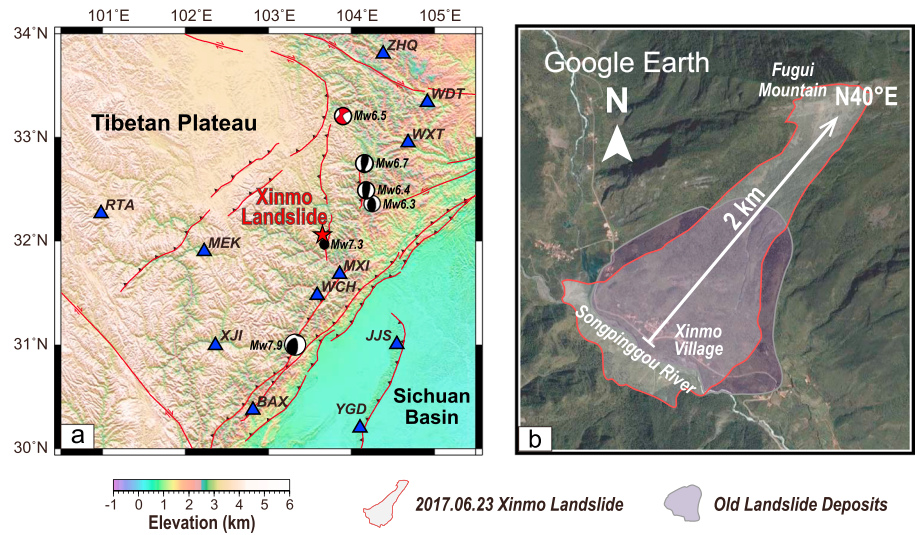
Figure 1. (a) Topographic and tectonic map of the Xinmo landslide (red star). Blue triangles denote seismic stations used in this study, and red lines mark the major faults. Beach balls denote the locations and focal mechanisms of five strong earthquakes before (black compressional quadrant) and after (red compressional quadrant) the landslide in this area, and the black dot represents the location of the 1933 Diexi earthquake without determined focal mechanism (source: global centroid moment catalog (gCMT), http://www.globalcmt.org; National Earthquake Information Center (NEIC), http://earthquake.usgs.gov). (b) The satellite image before the landslide (source: Google Earth). The gray area with a red solid line depicts the spatial ranges of the Xinmo landslide. The purple area with a gray solid line denotes the location of the old landslide deposits.
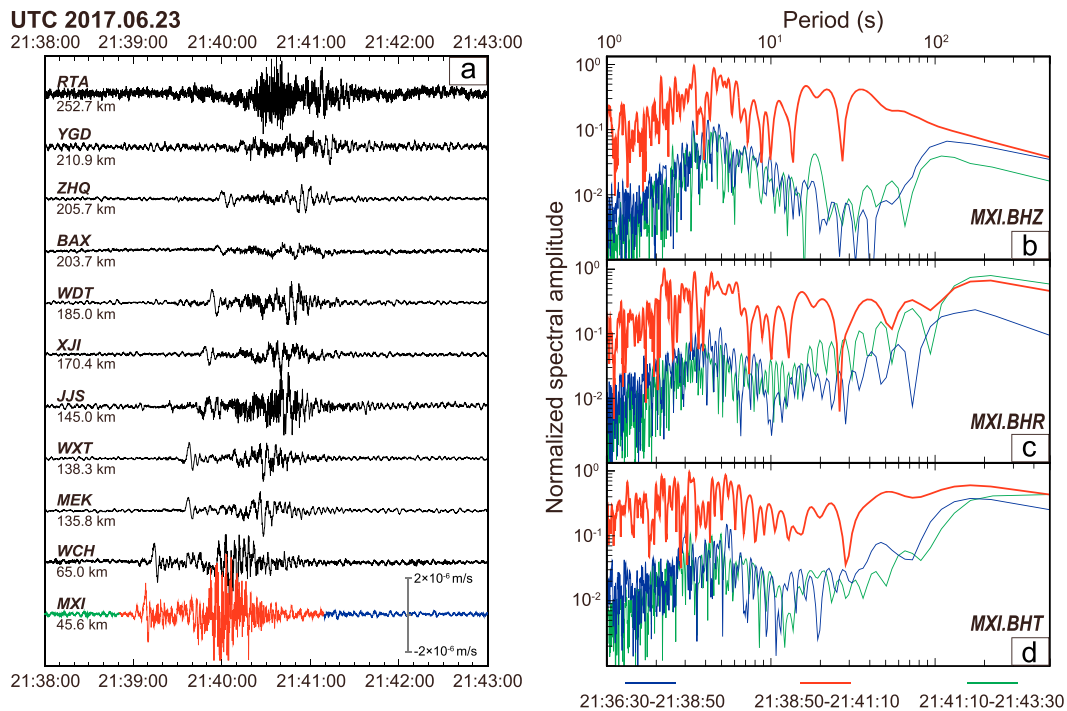

Figure 2. (a) Low-pass-filtered (<5 Hz) vertical component waveforms used in this study are plotted on the same scale as shown in the map. Station codes and distances to the landslide site are given at the left of each trace. (b–d) Normalized spectral amplitude of vertical (BHZ), radial (BHR), and transverse (BHT) components recorded at MXI station. And colors indicate different time ranges within 140-s durations, red for landslide signals, blue for noises before signals, and green for noises after signals, similar as the colored vertical component waveform of MXI station in (a).

BBVS-60 60 s—50 Hz) for the inversion of the force-time function (e.g., Allstadt, 2013; Chao et al., 2016; Ekström & Stark, 2013; Gualtieri & Ekström, 2018; Hibert et al., 2014; Lin et al., 2010; Yamada et al., 2013). Seismic records are first preprocessed by removing instrument responses, integrating to displacements, resampling to 1 Hz, and rotating horizontal components to radial and transverse directions. Then, considering the falloff in response curves of seismometers (Figures 2b–2d), a phase-free (acausal) band-pass filter with frequency range of 0.01–0.05 Hz is applied to the rotated seismic records.

2.2. Method

The slide mass can be considered as a separated body from the solid Earth and its force acting on the solid Earth (F) can be approximately described as a single-force mechanism within the long-wavelength limit (Ekström & Stark, 2013; Fukao, 1995; Kanamori & Given, 1982; Takei & Kumazawa, 1994). Thus, this force has a reactive force in an opposite direction acting on the slide mass (F_s), as a resultant force of gravity, friction, and centripetal forces, which can be written as

$$F(t) = -F_s(t) = -ma(t) \tag{1}$$

where m is the mass and a is the acceleration of the slide mass.

The displacements at stations (d) for a realistic source can be obtained by convolving the Green's functions (G) with a force-time function being equivalent to the force acting on the solid Earth in the landslide event (Aki & Richards, 1980; Stein & Wysession, 2003):

$$d(t) = F(t)*G(t) \tag{2}$$

where the Green's functions $G(t)$ can be calculated using a generalized 1-D Earth model, for long-period signals have little sensitivities to small-scale heterogeneities of the Earth's structure. In this study, the 1-D layered half-space Earth model is constructed by a regional crustal model averaged from Crust 1.0 (Laske et al., 2013) and a reference mantle model from ak135 (Kennett et al., 1995). Owing to the facts that only long-period signals (20–100 s) are modeled in this study, and at long periods the fast and accurate computation is still valid for the generation of landslide's synthetic seismograms with sources and receivers at close to or the same depths near surface, the wave number integration method is used to calculate Green's functions (G) between each station and the landslide site (Herrmann, 2013; Wang & Herrmann, 1980; Zhang et al., 2003). Then, a damped least squares approach is used to invert the force-time function (F) in the time domain by fitting the long-period signals (d) generated by the landslide (Aki & Richards, 1980; Allstadt, 2013):

$$F = \left(G^{*T}G^* + \alpha^2 I\right)^{-1} G^{*T} d \tag{3}$$

where G^* represents the Green's function convolution matrix, G^{*T} indicates the transpose of G^*, and I is the identity matrix. The damping parameter α is chosen as providing the optimal trade-off between model norm and variance reduction of the data (Figure S1).

The momentum of the slide mass (p) can be estimated from integration of force acting on the slide mass:

$$p(t) = mv(t) = \int_0^t F_s(\tau)d\tau = -\int_0^t F(\tau)d\tau \tag{4}$$

The conservation of momentum should be considered in the inversion due to no force associated with the slide mass when at rest (Allstadt, 2013; Chao et al., 2016; Ekström & Stark, 2013; Gualtieri & Ekström, 2018). Due to the noise effects, the estimated force and momentum would not remain the same before and after sliding (Yamada et al., 2013). Therefore, we invert a finite duration of force-time function by constraining force and momentum of the slide mass to zero before and after the landslide.

By integrating the force twice, we could obtain the displacement of the slide mass (D), which is related to the mass of the slide mass:

$$D(t) = \frac{1}{m}\iint_0^t F_s(\tau)d\tau = -\frac{1}{m}\iint_0^t F(\tau)d\tau \tag{5}$$

This equation shows that the representative mass (m) can be estimated from the force acting on the solid Earth and the displacement of the slide mass. Therefore, constrained by the field observed displacement, the mass and dynamic parameters of the landslide can be estimated as long as the force-time function is known.

Adopting the mass and trajectory of slide mass, the apparent friction coefficient (μ) during sliding could be estimated as the following:

$$\mu = (\sin\theta - f/mg)/\cos\theta \tag{6}$$

where θ is the dip angle of the slope and f is the downslope force acting on the slide mass. Neglecting the centripetal force, f could be obtained from $\boldsymbol{F}(t)$.

Note that we cannot resolve the spatial distribution of the force because it was parameterized as an average single force acting on the solid Earth. Therefore, the mass, dynamic parameters, and apparent friction coefficient would reflect overall effects during sliding.

3. Results

3.1. Finite Duration of the Force-Time Function

Using the methods described above, we invert the seismic data to solve for the force-time function of the Xinmo landslide. Synthetic seismograms are computed by convolving the force-time function and Green's functions as described in equation (1). Cross-correlation coefficients and variance reductions between the observed and synthetic seismograms are calculated to estimate reliability of our inversion results (Figure 3).

We constrain the landslide's start time in the range of 21:38:47–21:38:53, considering an average group velocity of ~3.0 km/s computed by comparing arrival times of the long-period signals recorded at different stations (Figure S2). After testing the start time in this range, we chose 21:38:51 ($t = 51$ s in Figure 4) as the start time for the maximum average cross-correlation coefficients and variance reductions between observed and synthetic seismograms. The seismic signals' duration (Figure 2a) and the unconstrained inversion results (Figure 4, with flattened oscillations near to zero after about 100 s) both indicate that the landslide's duration would be ~100 s. Based on the inversion results computed with different end times ($t_f = 135$–175 s), we select $t_f = 155$ s as the landslide's end time, and this result not only presents main broadband transients of force-time function but also avoids artificially truncated signals (Figure 4). Finally, we recover a force-time function within 104-s duration ($t = 51$–155 s) of the landslide, and synthetic seismograms computed from our result are well fitted with observed ones with an average cross-correlation coefficients of 0.82 and variance reductions of 0.57, respectively (Figure 3). Even some signals which are not used in the inversion due to their low signal-to-noise ratios are also partly fitted with synthetic seismograms calculated from our result (Figure 3). The constrained force-time function, setting the force and momentum of the slide mass to zero at the rest before and after the landslide, is similar to the unconstrained one in the whole active stages of the landslide, indicating little effect induced by the noise before and after the landslide (Figure 4).

To further evaluate the stability of the inversion with our data, we randomly extract 15 channel signals from 22 ones used in this study to inverse a force-time function and repeat the random processes 100 times by a bootstrap resampling scheme (Efron & Tibshirani, 1986). These tests indicate that all the force-time functions are similar, and thus, the data we used are enough to achieve a stable inversion (Figure S3). We also investigate force-time functions inversed from different period-band data. Force-time functions are similar in amplitudes and phases when the 10–100- and 20–100-s period bands are included, but have a dramatic phase difference in vertical component when period bands longer than 30 s (Figure S4). This illustrates that the data in 20–100-s period band used in this study can recover main accelerating and decelerating processes of the landslide, and effectively avoid the influence of regional heterogeneous structures at the same time.

3.2. Features of the Force-Time Function

Considering that the mass sliding direction is nearly along N40°E direction (Figure 1b), we rotate horizontal force components to N40°E and N50°W directions. The small amplitude of the N50°W component
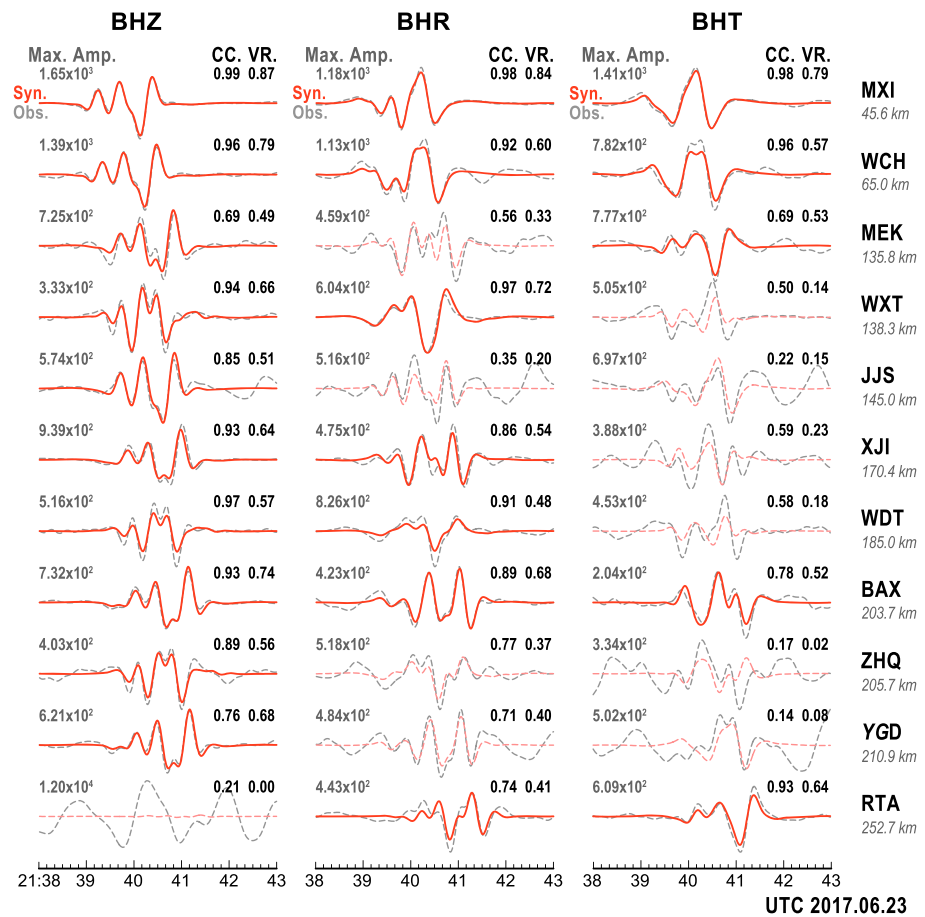
Figure 3. Observed (gray lines) and synthetic (red lines) long-period seismograms band-pass filtered between 20 and 100 s in vertical (BHZ), radial (BHR), and transverse (BHT) components. Solid lines represent high signal-to-noise ratio waveforms used in the final inversion, and dashed lines represent deleted ones in the inversion due to low signal to noise ratios. Cross-correlation coefficients (CC) and variance reductions (VR) between observed and synthetic seismograms are shown at the right of each trace, and maximum amplitudes with the unit of nanometers are shown at the left. Station codes and components are shown at the right and top, respectively.

indicates that mass movement is actually secondary in this direction. The N40°E and vertical components have coherent fluctuations and reach their peak amplitudes on the order of 10^{10} N at $t = 110$–120 s (Figure 5a). The momentum and displacement of the slide mass, obtained from the equations (4) and (5), also show that the mass movements are mainly in N40°E and vertical direction (Figures 5b and 5c), except for a notable increase of displacement in the N50°W direction and a vertical rebound after $t = 120$ s (Figure 5c).

Spectra of the force-time function show similar shapes with corner periods (T_0) in three components, and are nearly proportional to T^2 and T^{-1} at periods shorter and longer than corner periods, respectively (Figure 6). Similar trends are also revealed by previous studies on the theoretical and observed spectra of landslide sources (Gualtieri & Ekström, 2018; Kawakatsu, 1989; Okal, 1990), which are distinct from regular earthquakes with flattened spectra at periods longer than corner periods. As shown in Figure 6, the N40°E and vertical components' spectra have similar corner periods around $T_0 = 80$ s, and the N50°W component's spectrum has a corner period around $T_0 = 55$ s. The corner period reflects the duration of landslide's mainly accelerating and decelerating cycle which can excite significant long-period signals. In this study, we include spectra's corner periods of the force-time function in the filter band (20–100 s) of signals used in the inversion, which could avoid underestimation on force magnitude due to incomplete recovery of landslide's main accelerating and decelerating cycle (Gualtieri & Ekström, 2018).
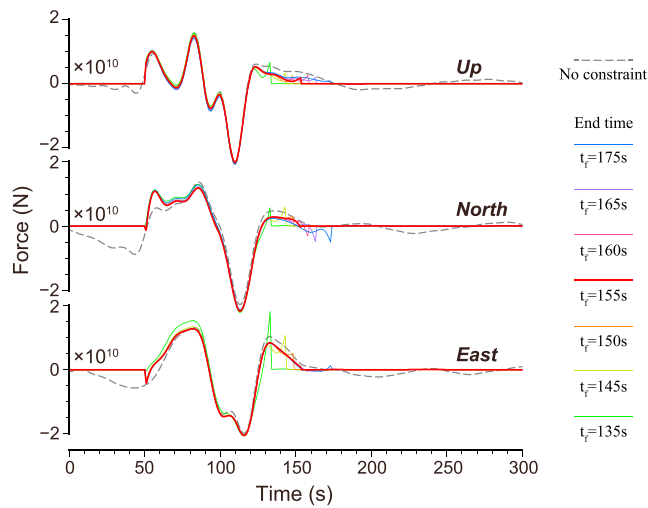
Figure 4. The force-time function in vertical, north, and east components, positive in up, north, and east. Gray dashed lines show results from the unconstrained inversion. Colored solid lines show results with same start time (t = 51 s) but different end time constrains (t_f), and red ones represent final results of this study which selected the end time at t = 155 s. The start time of the force-time function is at 21:38:00, 23 June 2017, UTC.

3.3. Main Dynamic Parameters

The force derived from the vertical and horizontal (N40°E) components shows that the force acting on the solid Earth has a direction along the updip direction of the slope at t = 51–93 s represents the accelerating stage (stage 1) of the slide mass (Figures 7a and 8c). The momentum also shows continuous increasing with a direction along the slope in this stage, and reaches the maximum value of 5.29×10^{11} kg·m/s at the end of this stage (Figures 7b and 8d). In the decelerating stage (stage 2, t = 93–126 s), the force has a reversed direction from that in the stage 1 (Figures 5a and 7a), and reaches a peak amplitude of 3.94×10^{10} N at t = 113 s (Figure 8c). The accelerating (stage 1) and decelerating (stage 2) cycle depicts a landslide's dynamic history as shown in other landslides' studies (e.g., Ekström & Stark, 2013; Gualtieri & Ekström, 2018; Hibert et al., 2014; Yamada et al., 2013). During the stage 3 (t = 126–155 s) in our result, the force has relatively small amplitudes associated with the depositing stage of the landslide (Figures 5a and 7a). A significant horizontal deviation and vertical rebound of the force's center after t = 120 s (Figures 7c and 7d) may indicate more variability than general plastic deformation or scattered accumulation as revealed by other studies (e.g., Ekström & Stark, 2013; Hibert et al., 2014; Yamada et al., 2013). The 104-s duration of the force-time function revealed by our results is ~20 s longer than corner periods of N40°E and vertical force components' spectra (Figures 5a and 6), and these differences also indicate more complicated processes in this event than the simple accelerating and decelerating cycle revealed by other landslides' studies.

Our results show that the trajectory of force's center has a nearly N40°E direction and 25° dip angle during main sliding stage when the slide mass reaches a high speed (Figures 7c and 7d), which is consistent with the filed observation shown in the Figure 1b (Fan, Xu, et al., 2017). We adjust the representative mass of the slide mass to ensure the horizontal and vertical displacement scales fitting to the field observed runout distance (~2.4 km), and finally obtain the constant mass of 9×10^9 kg. Considering the estimated slide mass, the mass would reach its maximum absolute velocity of 58.8 m/s and acceleration of 4.38 m/s² at t = 93 s and t = 113 s after the landslide started, respectively (Figures 8c and 8d). Assuming a density of the deposits of 2.0–2.5×10^3 kg/m³, the inferred volume is 3.6–4.5×10^6 m³, which is similar to the value (4.5×10^6 m³) obtained by ground observations and digital elevation model analysis (Fan, Xu, et al., 2017). Some discrepancies may stem from that the hypothesis of the single-force mechanism does not include additional aseismic transport of material (Hibert et al., 2014). Moreover, the crushed and new involved masses are not effectively estimated during sliding, and thus, the constant mass assumption would be not valid strictly. To investigate the effect of the inconstant mass on the sliding process, we estimate the trajectories of the force's center with different mass of 7, 9, and 11×10^9 kg (Figure S5), and the tests show similar main sliding directions but decreased displacements with mass increasing. These features indicate that the main sliding processes revealed by the force-time function would be little affected by the inconstant mass with limited variations. While the amplitudes of dynamic parameters, such as accelerations, velocities, and displacements, would decrease when much more mass is involved at the last stage of the sliding.

4. Discussion

Force-time function inversed from long-period signals depicts bulk momentum variations, while high-frequency signals, another main frequency band in spectra of landslide's signals (Figures 2b–2d), reflect small-scale momentum exchanges. Overall analysis of the landslide's dynamic parameters with high-frequency seismic signal features provides more information about the landslide's motion (Allstadt, 2013; Hibert et al., 2014; Yamada et al., 2013). Therefore, we shift absolute force-time function, absolute momentum, and apparent friction coefficient by the approximate long-period signal's travel time of 15 s between the landslide site and MXI station (Figure S2), and compare with the seismic signals and its spectrogram recorded at the MXI station (Figures 8a and 8b). We divide the dynamic processes of the landslide into
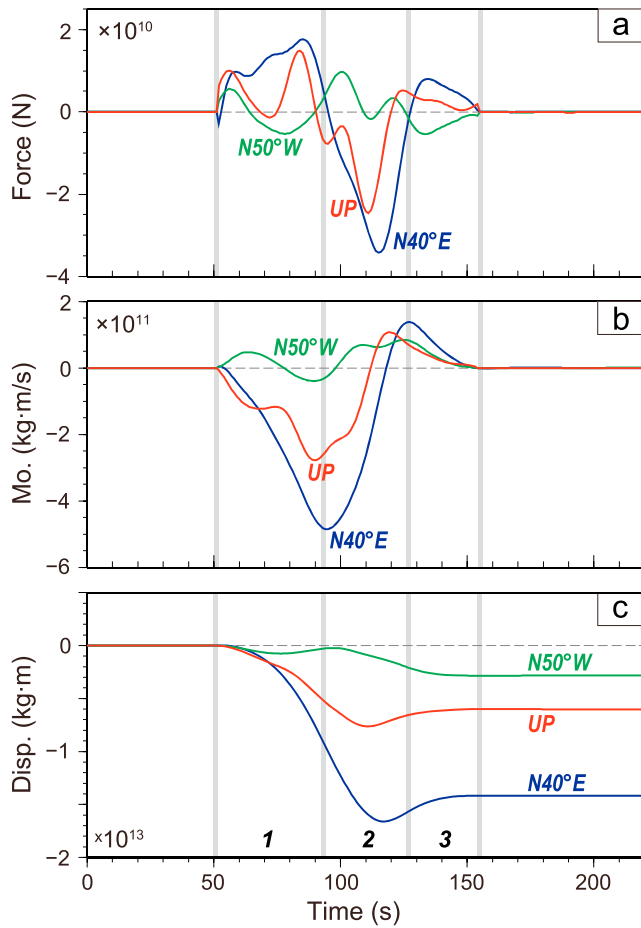
Figure 5. (a) The rotated force-time function, (b) estimated momentum, and (c) displacement of force's center in vertical, N40°E, and N50°W components with constraints before and after the landslide, positive in up, N40°E, and N50°W directions.
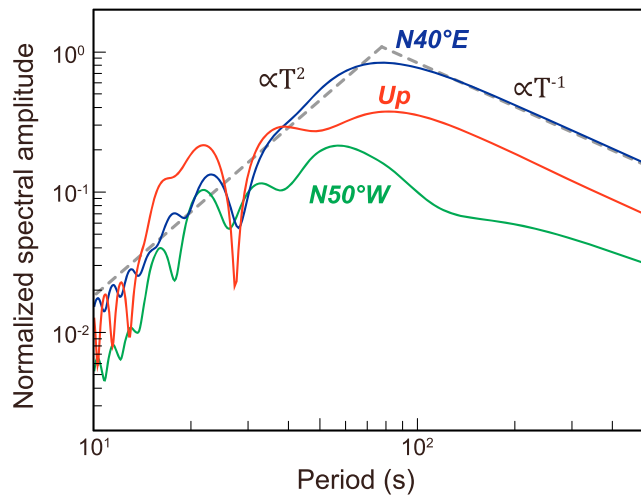

Figure 6. Normalized spectral amplitude of the force-time function in vertical, N40°E, and N50°W components. The gray dashed line shows a reference spectrum which is proportional to T^2 and T^{-1} at periods short and longer than corner periods, respectively.

three stages: $t = 51–93$, $93–126$, and $126–155$ s, representing accelerating, decelerating, and depositing processes of the landslide (Figures 5 and 8).

4.1. Accelerating Stage: High-Position Rockslide and Rapid Long-Runout Debris

During the stage 1, the accelerating process is significantly divided into two cycles ($t = 51–68$, $75–93$ s), especially in the vertical component (Figures 5a and 8c). And ~10-s impulse onset of seismic signals indicates a strong elastic rebound at the initiation of the landslide (Figures 2a and 8a), which is significantly different from other landslide signals (e.g., Dammeier et al., 2011; Deparis et al., 2008; Hibert et al., 2011; Suriñach et al., 2005). Field observation find that the landslide source area is a typical bedding slope mainly consisted of metasandstones and slates with an attitude of 190° ∠ 47° and two sets of joints (134° ∠ 84° and 316° ∠ 47°), and high-resolution satellite imagery reveals three steep dip cracks along the sliding direction of the landslide (Fan, Xu, et al., 2017; Xu et al., 2017; Yin et al., 2017). After a long time of deformation and significant reduction in strength due to more intense rainfall in the same period in this area, the landslide source suddenly slides as a whole block controlled by these structures (Fan, Xu, et al., 2017; Intrieri et al., 2018). Therefore, the first accelerating cycle of the stage 1 and impulse onset of seismic signals depict a high-position rockslide process with maximum acceleration of 1.43 m/s^2 ($t = 57$ s), and this process would provide enough kinetic energy to induce a series of subsequent hazards.

Frictional weakening with increasing slip velocity is observed in fast sliding experiments of rocks (Di Toro et al., 2011; Spagnuolo et al., 2016; Wang et al., 2017; Yao et al., 2016) and invoked to explain key features of earthquake and landslide (Di Toro et al., 2011; Lucas et al., 2014). Our results show that the apparent friction coefficient drops from 0.56 to 0.34 as velocity increases to 19.7 m/s during the first accelerating cycle, and then remains at 0.3~0.34 with velocity continuously increasing during the second accelerating cycle (Figure 8e). During the decelerating stage, the apparent friction coefficient has an increasing trend (Figure 8e), but it should be noted that its magnitude might be overestimated due to mass increasing and dip angle decreasing at the end of the sliding. The apparent friction coefficient deduced in this study has a fluctuation similar as other landslides' basal friction estimated from seismic data (e.g., Allstadt, 2013; Brodsky et al., 2003; Gualtieri & Ekström, 2018; Yamada et al., 2013), but remains at low level for a relative long duration (~25 s in this study versus ~15 s in Yamada et al. (2013)). The apparent friction coefficient is considered as the effects of both true friction coefficient (μ') and basal fluid pressure (P; Iverson, 1997):

$$\mu\sigma_n = \mu'(\sigma_n - P) \qquad (7)$$

where σ_n is the normal stress at the base of the sliding mass. Based on this hypothesis, considering true friction coefficients of different rock categories are greater than 0.6 (e.g., Byerlee, 1978; Di Toro et al., 2011; Spagnuolo et al., 2016), this low apparent friction coefficient suggests that basal fluid pressures were at least 43% of basal normal stress. During two months before the Xinmo landslide occurred, the antecedent rainfall in Diexi town reaches 200 mm, which is 42% more than the same periods in previous years (Fan, Xu, et al., 2017; Wang et al., 2018). Such durative heavy rainfall would cause noticeable
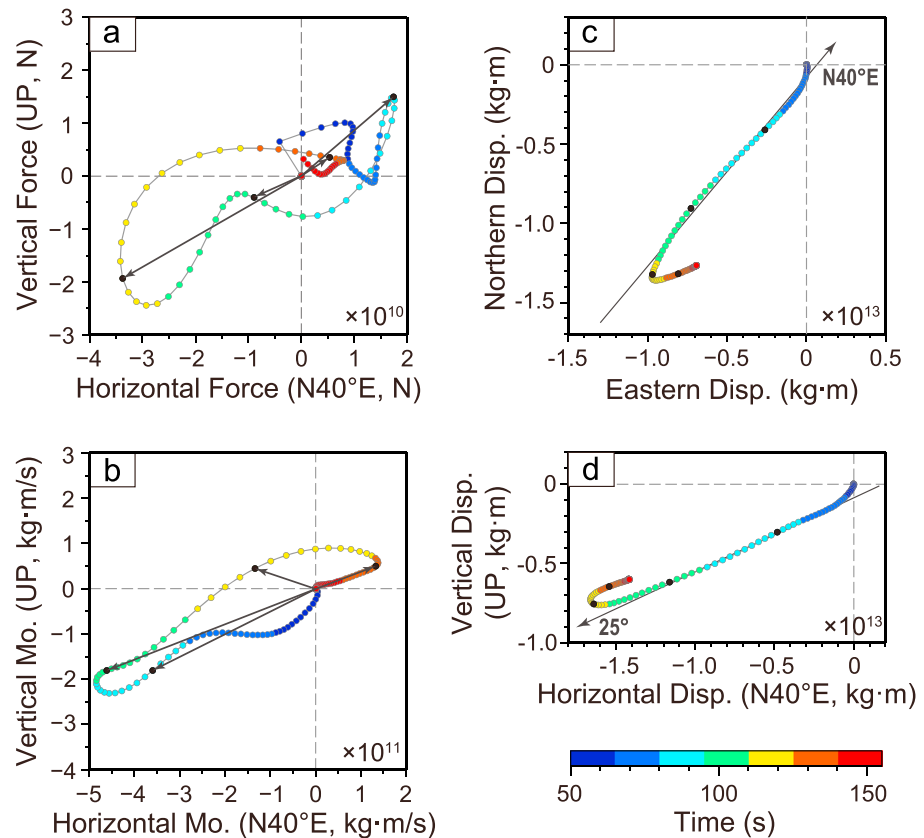
Figure 7. (a and b) Particle motion of the force-time function and the estimated momentum in the vertical plane along N40°E direction. Dots represent each second of time, and colors denote different time range. Black arrows represent directions and magnitudes of force and momentum at $t = 85, 100, 115,$ and 130 s. (c and d) Horizontal and vertical (N40°E direction) trajectory of the force's center. Black arrows represent N40°E direction in the horizontal plane and 25° dip angle in the vertical plain. Black dots represent location of the force's center at $t = 85, 100, 115,$ and 130 s.

increases in the basal fluid pressures on the metasandstones slope fractured by previous intense seismic activities. These geological and meteorological conditions would contribute to a relatively long duration of low apparent friction coefficient of the Xinmo landslide, and eventually induce the rapid long-runout debris with maximum velocity of 58.8 m/s and runout distance of 2.4 km.

4.2. Decelerating and Depositing Stages: Reactivation of Preexisting Deposition Fan

The stage 2 has a rapid decrease in the momentum along the N40°E direction with maximum deceleration of -4.38 m/s^2 ($t = 113$ s; Figures 5b, 8c, and 8d). And the slide mass reaches the open terrain during this stage, as revealed by the trajectory fitted to field observations (Figures 9a and 9b), indicating that the deceleration of the slide mass is associated with the increases of hindrance from supporting force and friction. At the same time, corresponding seismic signals contain intense high-frequency components (Figures 8a and 8b), which indicates granular collisions in the decelerating slide mass due to the strong impact force in the deceleration of the slide mass (Ekström & Stark, 2013; Hibert et al., 2011, 2017; Schneider et al., 2010). The hindrance force would have a typical increase and decrease cycle while the slide mass decelerates to rest (Brodsky et al., 2003). However, in our results, the hindrance force experiences an interrupted process with double cycles divided by a significant short-term decrease ($t = 96$–101 s) in the vertical component (Figures 5a and 7a). As revealed by satellite images and field observations, the deposit area of the 2017 Xinmo landslide is actually covered by a deposition fan of a landslide induced by the 1933 Diexi earthquake (Figures 1b and 9b; Fan, Xu, et al., 2017; Xu et al., 2017). The old deposition fan would be reactivated by the huge momentum of the new landslide, and that would result in a large area of fresh bedrock being exposed where once covered by old deposits (Figures 9a and 9b). And in this process, the force center acting on the solid Earth would
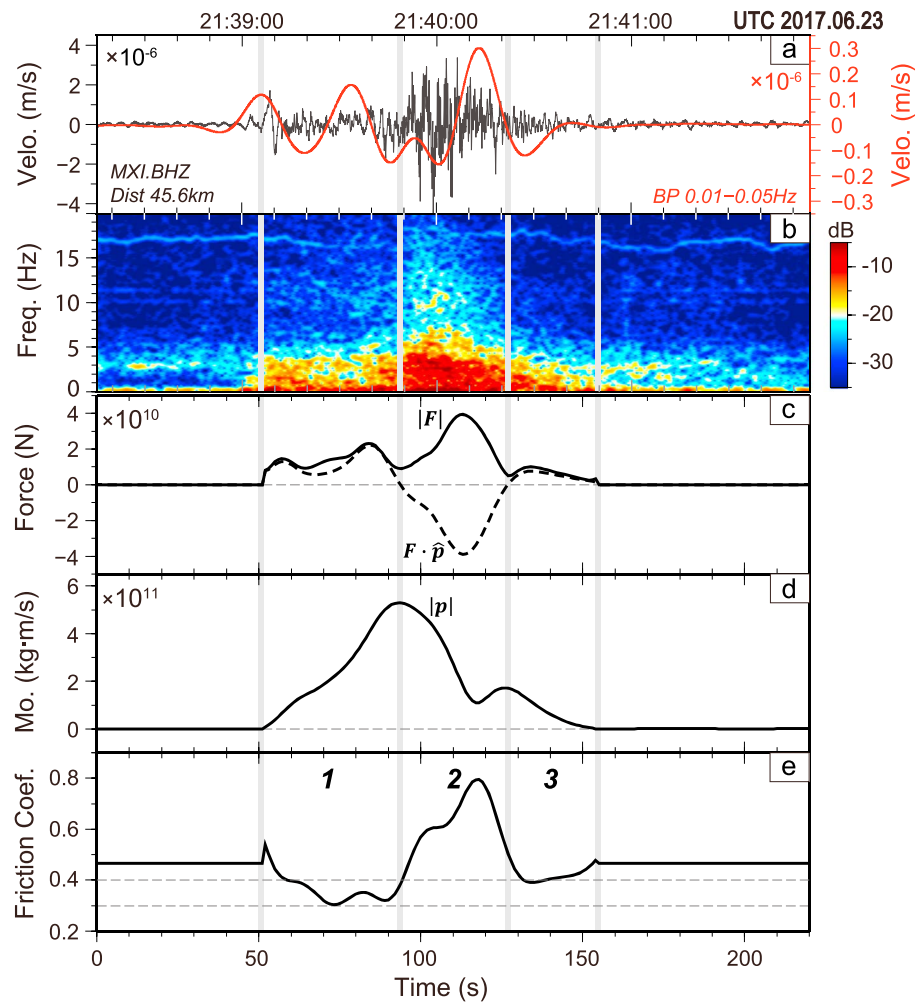
Figure 8. (a) The raw (black) and 0.01–0.05-Hz band-pass-filtered (red) vertical component seismograms recorded at the MXI station. (b) Spectrogram of the vertical component seismic signal recorded at the MXI station. (c) Estimated absolute force (solid line) and the force in the direction of the momentum (dashed line) obtained by computing the vector inner product between the force and normalized velocity ($\boldsymbol{F}\cdot\hat{\boldsymbol{p}}$). (d) Estimated absolute momentum of the center of slide mass. (e) Estimated friction coefficient varying with time. Perpendicular gray lines indicate transitions between different stages (1, 2, and 3).

deviate from the bottom of the new slide mass (Figure 9c; $t{\sim}100$ s) to the bottom of the old deposition fan (Figure 9c; $t{\sim}115$ s). Therefore, the preexisting deposition fan would act as a buffer layer in the decelerating process of the new landslide, and interrupt the increase and decrease cycle of the hindrance force.

During the stage 3, the mass movements are mainly along the updip direction of the slop with a relatively small force amplitude (Figures 7a and 7b), which is associated with general plastic deformation or scattered accumulation in the depositing process of the landslide as revealed by other studies (e.g., Hibert et al., 2014; Yamada et al., 2013). While in this study, the force's center has a significant deviation in vertical and horizontal direction after $t = 120$ s (Figures 7c and 7d). As discussed above, the old deposition fan would be reactivated during the decelerating process, and then the deposits would be compacted and stop moving with increasing of the hindrance force. While the apparent friction coefficient decreases again during the stage 3 (Figure 8e), which indicates that the new slide mass may keep moving over the top of the old deposition fan due to the huge momentum. As revealed by field observations, a preexisting ravine cause the new slide mass to deviate eastward in the transportation stage, and form an asymmetrical deposition with high eastern side in the U-shaped channel (Figure 9a; Fan, Xu, et al., 2017; Xu et al., 2017; Yin et al., 2017). Therefore, the
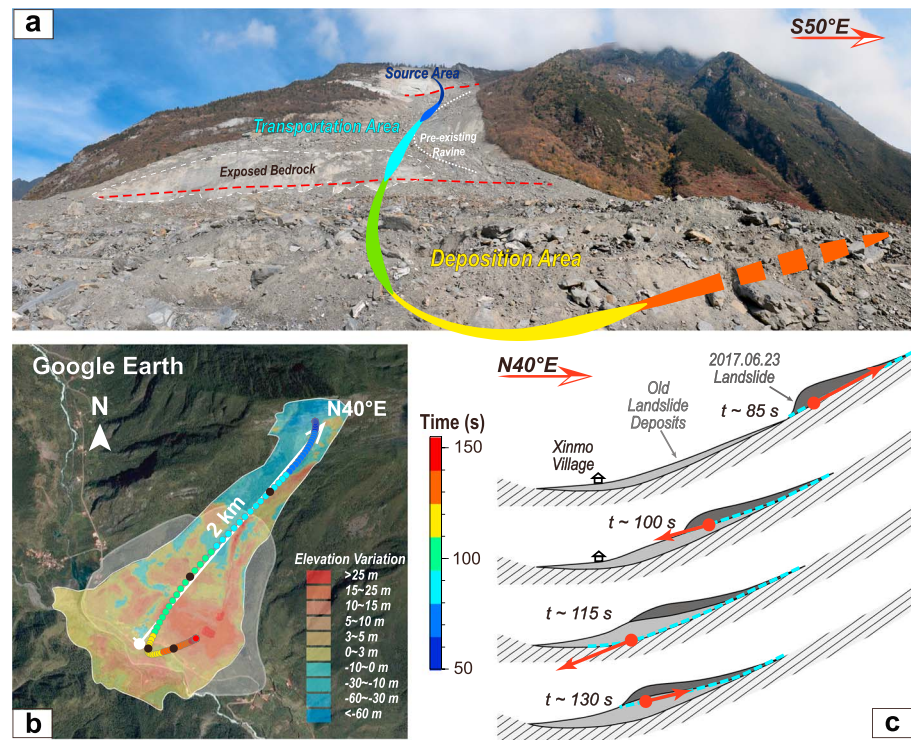
Figure 9. (a) An overview photo of the Xinmo landslide. The source, transportation, and deposition areas are separated by red dashed lines, and the preexisting ravine and newly exposed bedrock are indicated with white dashed lines. To approximately correlate the realistic observations with the main stages of the sliding processes constrained by seismic signals analysis, the reference trajectory of the center of slide mass as shown in (b) is shown by solid lines with different colors denoting different time ranges after the landslide started. (b) Horizontal trajectory of the force's center with the starting point at where has a maximum elevational reduction in the source area and a reference mass of 9×10^9 kg. Dots show the location of the force's center per second, with different colors denoting different time range. The translucent color area depicts elevation variations before and after the landslide (source: Fan, Zhang, et al., 2017). The gray area denotes the location of the old deposition fan. The black dots represent the location of the force's center at $t = 85, 100, 115,$ and 130 s, and the white dot represents the location where the photo (a) was taken. (c) An interpretive model of the vertical deviation of force's center caused by the old deposition fan. The red arrows represents the variation of the magnitude and direction of the force acting on the Earth surface in different stages similar as black ones in the Figure 7a. When the slide mass accelerating ($t \sim 85$ s) and decelerating ($t \sim 100$ s) in the propagation stage, the force has a center at the bottom of the new slide with an opposite direction to the acceleration. Reacted by the huge momentum, the old deposition fan would move with the new slide mass, and the force's center would be changed to the bottom of the old deposition fan ($t \sim 115$ s). With the increasing of the hindrance force, the old deposition fan would be compacted until stop moving. While, the new slide mass and some entrained loose old deposits would keep moving over the top of the old deposition fan, and thus, the force center would be transited back to the bottom of the new combined slide mass ($t \sim 130$ s).

force's center would be transited back to the bottom of the moving slide mass during the stage 3, which would be shown as a vertical rebound (Figure 9c; $t\sim130$ s) and a horizontal deviation to the depositing central area where would be the end of the new slide mass' trajectory (Figure 9b).

Based on quantitative measurements extracted from the seismic data in this study, the Xinmo landslide is characteristic of a typical chain-style landslide hazardous process (Yin et al., 2017): initiated by a high-position rockslide which is controlled by the structures in the source area and steep topography, followed by a rapid long-runout debris benefitted from the significant increase of basal fluid pressure after long-term rainfall, and the reactivation of the preexisting deposition fan caused by the huge momentum of the new landslide lead to the escalation of catastrophic disasters.

5. Conclusions

In this study, we analyze seismic signals generated by the Xinmo landslide and inverse the force-time function within 104-s duration of the event. Together with postslide evidences from field observations, our results

provide information on sliding sequence and dynamic parameters of the landslide. By adjusting the trajectory of the force's center based on field observations, we further estimate that the mass of the landslide is about 9.0×10^9 kg, and corresponding maximum absolute velocity and acceleration of the center of slide mass are 58.8 m/s and 4.38 m/s^2, respectively.

Through overall analysis of the landslide's dynamic parameters, apparent friction coefficient, and high-frequency seismic signal features, we recover a three-stage process: acceleration ($t = 51–93$ s), deceleration ($t = 93–126$ s), and deposition ($t = 126–155$ s) of the landslide, and provide key insights into the mechanisms controlling the landslide's motion at different stages. Multiple preconditions on geological and meteorological time scales induce the chain-style landslide hazardous process. In particular, the basal fluid pressure increase and preexisting deposition fan contribute to the serious and extensive damage. Therefore, based on qualitatively constrained relations between multiple preconditions and rapid process of the landslide from seismic signals, comprehensively recognizing potential instabilities in the geological hazard assessment and efficiently developing real-time technology for early warning of landslide would contribute to mitigating catastrophic landslides.

References

Aki, K., & Richards, P. G. (1980). *Quantitative Seismology: Theory and Methods*. San Francisco, CA: W.H. Freeman.

Allstadt, K. (2013). Extracting source characteristics and dynamics of the August 2010 Mount Meager landslide from broadband seismograms. *Journal of Geophysical Research: Earth Surface*, *118*, 1472–1490. https://doi.org/10.1002/jgrf.20110

Brodsky, E. E., Gordeev, E., & Kanamori, H. (2003). Landslide basal friction as measured by seismic waves. *Geophysical Research Letters*, *30*(24), 2236. https://doi.org/10.1029/2003GL018485

Byerlee, J. (1978). Friction of rocks. *Pure and Applied Geophysics*, *116*(4), 615–626. https://doi.org/10.1007/bf00876528

Chao, W. A., Wu, Y. M., Zhao, L., Chen, H., Chen, Y. G., Chang, J. M., & Lin, C. M. (2017). A first near real-time seismology-based landquake monitoring system. *Scientific Reports*, *7*, 43510. https://doi.org/10.1038/srep43510

Chao, W. A., Zhao, L., Chen, S. C., Wu, Y. M., Chen, C. H., & Huang, H. H. (2016). Seismology-based early identification of dam-formation landquake events. *Scientific Reports*, *6*, 19259. https://doi.org/10.1038/srep19259

Clark, M. K., House, M. A., Royden, L. H., Whipple, K. X., Burchfiel, B. C., Zhang, X., & Tang, W. (2005). Late Cenozoic uplift of southeastern Tibet. *Geology*, *33*(6), 525–528. https://doi.org/10.1130/g21265.1

Cruden, D. M., & Varnes, D. J. (1996). Landslides types and processes. In A. K. Turner & R. L. Schuster (Eds.), *Landslides: Investigation and Mitigation* (pp. 36–75). Washington, DC: Transportation Research Board.

Dammeier, F., Moore, J. R., Haslinger, F., & Loew, S. (2011). Characterization of alpine rockslides using statistical analysis of seismic signals. *Journal of Geophysical Research*, *116*, F04024. https://doi.org/10.1029/2011JF002037

Deparis, J., Jongmans, D., Cotton, F., Baillet, L., Thouvenot, F., & Hantz, D. (2008). Analysis of rock-fall and rock-fall avalanche seismograms in the French Alps. *Bulletin of the Seismological Society of America*, *98*(4), 1781–1796. https://doi.org/10.1785/0120070082

Di Toro, G., Han, R., Hirose, T., de Paola, N., Nielsen, S., Mizoguchi, K., et al. (2011). Fault lubrication during earthquakes. *Nature*, *471*(7339), 494–498. https://doi.org/10.1038/nature09838

Dong, J., Zhang, L., Li, M., Yu, Y., Liao, M., Gong, J., & Luo, H. (2018). Measuring precursory movements of the recent Xinmo landslide in Mao County, China with Sentinel-1 and ALOS-2 PALSAR-2 datasets. *Landslides*, *15*(1), 135–144. https://doi.org/10.1007/s10346-017-0914-8

Efron, B., & Tibshirani, R. (1986). Bootstrap methods for standard errors, confidence intervals, and other measures of statistical accuracy. *Statistical Science*, *1*(1), 54–77.

Ekström, G., & Stark, C. P. (2013). Simple scaling of catastrophic landslide dynamics. *Science*, *339*(6126), 1416–1419. https://doi.org/10.1126/science.1232887

Fan, J., Zhang, X. Y., Su, F. H., Ge, Y. G., Tarolli, P., Yang, Z. Y., et al. (2017). Geometrical feature analysis and disaster assessment of the Xinmo landslide based on remote sensing data. *Journal of Mountain Science*, *14*(9), 1677–1688. https://doi.org/10.1007/s11629-017-4633-3

Fan, X., Xu, Q., Scaringi, G., Dai, L., Li, W., Dong, X., et al. (2017). Failure mechanism and kinematics of the deadly June 24th 2017 Xinmo landslide, Maoxian, Sichuan, China. *Landslides*, *14*(6), 2129–2146. https://doi.org/10.1007/s10346-017-0907-7

Fu, B., Shi, P., Guo, H., Okuyama, S., Ninomiya, Y., & Wright, S. (2011). Surface deformation related to the 2008 Wenchuan earthquake, and mountain building of the Longmen Shan, eastern Tibetan Plateau. *Journal of Asian Earth Sciences*, *40*(4), 805–824. https://doi.org/10.1016/j.jseaes.2010.11.011

Fukao, Y. (1995). Single-force representation of earthquakes due to landslides or the collapse of caverns. *Geophysical Journal International*, *122*(1), 243–248. https://doi.org/10.1111/j.1365-246X.1995.tb03551.x

Gualtieri, L., & Ekström, G. (2017). Seismic reconstruction of the 2012 Palisades rockfall using the analytical solution to Lamb's problem. *Bulletin of the Seismological Society of America*, *107*(1), 63–71. https://doi.org/10.1785/0120160238

Gualtieri, L., & Ekström, G. (2018). Broad-band seismic analysis and modeling of the 2015 Taan Fjord, Alaska landslide using Instaseis. *Geophysical Journal International*, *213*(3), 1912–1923. https://doi.org/10.1093/gji/ggy086

Herrmann, R. B. (2013). Computer programs in seismology: An evolving tool for instruction and research. *Seismological Research Letters*, *84*(6), 1081–1088. https://doi.org/10.1785/0220110096

Hibert, C., Ekström, G., & Stark, C. P. (2014). Dynamics of the Bingham canyon mine landslides from seismic signal analysis. *Geophysical Research Letters*, *41*, 4535–4541. https://doi.org/10.1002/2014GL060592

Hibert, C., Ekström, G., & Stark, C. P. (2017). The relationship between bulk-mass momentum and short-period seismic radiation in catastrophic landslides. *Journal of Geophysical Research: Earth Surface*, *122*, 1201–1215. https://doi.org/10.1002/2016JF004027

Hibert, C., Mangeney, A., Grandjean, G., & Shapiro, N. M. (2011). Slope instabilities in Dolomieu crater, Réunion Island: From seismic signals to rockfall characteristics. *Journal of Geophysical Research*, *116*, F04032. https://doi.org/10.1029/2011JF002038

Intrieri, E., Raspini, F., Fumagalli, A., Lu, P., del Conte, S., Farina, P., et al. (2018). The Maoxian landslide as seen from space: Detecting precursors of failure with Sentinel-1 data. *Landslides*, *15*(1), 123–133. https://doi.org/10.1007/s10346-017-0915-7

Iverson, R. M. (1997). The physics of debris flows. *Reviews of Geophysics*, *35*(3), 245–296. https://doi.org/10.1029/97RG00426

Iverson, R. M., Reid, M. E., Iverson, N. R., LaHusen, R. G., Logan, M., Mann, J. E., & Brien, D. L. (2000). Acute sensitivity of landslide rates to initial soil porosity. *Science*, *290*(5491), 513–516. https://doi.org/10.1126/science.290.5491.513

Kanamori, H., & Given, J. W. (1982). Analysis of long-period seismic waves excited by the May 18, 1980, eruption of Mount St. Helens—A terrestrial monopole? *Journal of Geophysical Research*, *87*(B7), 5422–5432. https://doi.org/10.1029/JB087iB07p05422

Kawakatsu, H. (1989). Centroid single force inversion of seismic waves generated by landslides. *Journal of Geophysical Research*, *94*(B9), 12,363–12,374. https://doi.org/10.1029/JB094iB09p12363

Keefer, D. K., & Larsen, M. C. (2007). Assessing landslide hazards. *Science*, *316*(5828), 1136–1138. https://doi.org/10.1126/science.1143308

Kennett, B. L. N., Engdahl, E. R., & Buland, R. (1995). Constraints on seismic velocities in the earth from traveltimes. *Geophysical Journal International*, *122*(1), 108–124. https://doi.org/10.1111/j.1365-246X.1995.tb03540.x

Laske, G., Masters, G., Ma, Z., & Pasyanos, M. (2013). Update on CRUST1.0—A 1-degree global model of Earth's crust. In EGU General Assembly Conference. Edited.

Lin, C. H., Kumagai, H., Ando, M., & Shin, T. C. (2010). Detection of landslides and submarine slumps using broadband seismic networks. *Geophysical Research Letters*, *37*, L22309. https://doi.org/10.1029/2010GL044685

Liu, Z., Tian, X., Gao, R., Wang, G., Wu, Z., Zhou, B., et al. (2017). New images of the crustal structure beneath eastern Tibet from a high-density seismic array. *Earth and Planetary Science Letters*, *480*, 33–41. https://doi.org/10.1016/j.epsl.2017.09.048

Lucas, A., Mangeney, A., & Ampuero, J. P. (2014). Frictional velocity-weakening in landslides on Earth and on other planetary bodies. *Nature Communications*, *5*, 3417. https://doi.org/10.1038/ncomms4417

Molnar, P., & Tapponnier, P. (1975). Cenozoic tectonics of Asia: Effects of a continental collision. *Science*, *189*(4201), 419–426. https://doi.org/10.1126/science.189.4201.419

Okal, E. A. (1990). Single forces and double-couples: A theoretical review of their relative efficiency for the excitation of seismic and tsunami waves. *Journal of Physics of the Earth*, *38*(6), 445–474. https://doi.org/10.4294/jpe1952.38.445

Petley, D. N. (2013). Characterizing giant landslides. *Science*, *339*(6126), 1395–1396. https://doi.org/10.1126/science.1236165

Ren, J., Xu, X., Zhang, S., Yeats, R. S., Chen, J., Zhu, A., & Liu, S. (2018). Surface rupture of the 1933 *M* 7.5 Diexi earthquake in eastern Tibet: Implications for seismogenic tectonics. *Geophysical Journal International*, *212*(3), 1627–1644. https://doi.org/10.1093/gji/ggx498

Schneider, D., Bartelt, P., Caplan-Auerbach, J., Christen, M., Huggel, C., & McArdell, B. W. (2010). Insights into rock-ice avalanche dynamics by combined analysis of seismic recordings and a numerical avalanche model. *Journal of Geophysical Research*, *115*, F04026. https://doi.org/10.1029/2010JF001734

Spagnuolo, E., Nielsen, S., Violay, M., & Di Toro, G. (2016). An empirically based steady state friction law and implications for fault stability. *Geophysical Research Letters*, *43*, 3263–3271. https://doi.org/10.1002/2016GL067881

Stein, S., & Wysession, M. (2003). *An Introduction to Seismology, Earthquakes, and Earth Structure*. Malden, MA: Blackwell.

Suriñach, E., Vilajosana, I., Khazaradze, G., Biescas, B., Furdada, G., & Vilaplana, J. M. (2005). Seismic detection and characterization of landslides and other mass movements. *Natural Hazards and Earth System Sciences*, *5*(6), 791–798. https://doi.org/10.5194/nhess-5-791-2005

Takei, Y., & Kumazawa, M. (1994). Why have the single force and torque been excluded from seismic source models? *Geophysical Journal International*, *118*(1), 20–30. https://doi.org/10.1111/j.1365-246X.1994.tb04672.x

Wang, C. Y., & Herrmann, R. B. (1980). A numerical study of *P*-, SV-, and SH-wave generation in a plane layered medium. *Bulletin of the Seismological Society of America*, *70*(4), 1015–1036.

Wang, Y. F., Dong, J. J., & Cheng, Q. G. (2017). Velocity-dependent frictional weakening of large rock avalanche basal facies: Implications for rock avalanche hypermobility? *Journal of Geophysical Research: Solid Earth*, *122*, 1648–1676. https://doi.org/10.1002/2016jb013624

Wang, Y., Zhao, B., & Li, J. (2018). Mechanism of the catastrophic June 2017 landslide at Xinmo Village, Songping River, Sichuan Province, China *Landslides*, *15*(2), 333–345. https://doi.org/10.1007/s10346-017-0927-3

Wessel, P., Smith, W. H. F., Scharroo, R., Luis, J., & Wobbe, F. (2013). Generic Mapping Tools: Improved version released. *Eos, Transactions American Geophysical Union*, *94*(45), 409–410. https://doi.org/10.1002/2013EO450001

Xu, Q., Li, W., Dong, X., Xiao, X., Fan, X., & Pei, X. (2017). The Xinmocun landslide on June 24, 2017 in Maoxian, Sichuan: Characteristics and failure mechanism. *Chinese Journal of Rock Mechanics and Engineering*, *36*(11), 2612–2628. https://doi.org/10.13722/j.cnki.jrme.2017.0855

Yamada, M., Kumagai, H., Matsushi, Y., & Matsuzawa, T. (2013). Dynamic landslide processes revealed by broadband seismic records. *Geophysical Research Letters*, *40*, 2998–3002. https://doi.org/10.1002/grl.50437

Yao, L., Ma, S., Niemeijer, A. R., Shimamoto, T., & Platt, J. D. (2016). Is frictional heating needed to cause dramatic weakening of nano-particle gouge during seismic slip? Insights from friction experiments with variable thermal evolutions. *Geophysical Research Letters*, *43*, 6852–6860. https://doi.org/10.1002/2016gl069053

Yin, Y., Wang, W., Zhang, N., Yan, J., & Wei, Y. (2017). The June 2017 Maoxian landslide: Geological disaster in an earthquake area after the Wenchuan M_s 8.0 earthquake. *Science China Technological Sciences*, *60*(11), 1762–1766. https://doi.org/10.1007/s11431-017-9148-2

Zhang, H., Chen, X., & Chang, S. (2003). An efficient numerical method for computing synthetic seismograms for a layered half-space with sources and receivers at close or same depths. *Pure and Applied Geophysics*, *160*, 467–486. https://doi.org/10.1007/PL00012546

Zhang, Z., Wang, Y., Chen, Y., Houseman, G. A., Tian, X., Wang, E., & Teng, J. (2009). Crustal structure across Longmenshan Fault belt from passive source seismic profiling. *Geophysical Research Letters*, *36*, L17310. https://doi.org/10.1029/2009GL039580